

www.acsami.org Research Article

Finding Optimal Mid-Infrared Nonlinear Optical Materials in Germanates by First-Principles High-Throughput Screening and Experimental Verification

Jin Yu, Bingbing Zhang,* Xiaodong Zhang, Ying Wang,* Kui Wu, and Ming-Hsien Lee



Cite This: ACS Appl. Mater. Interfaces 2020, 12, 45023-45035



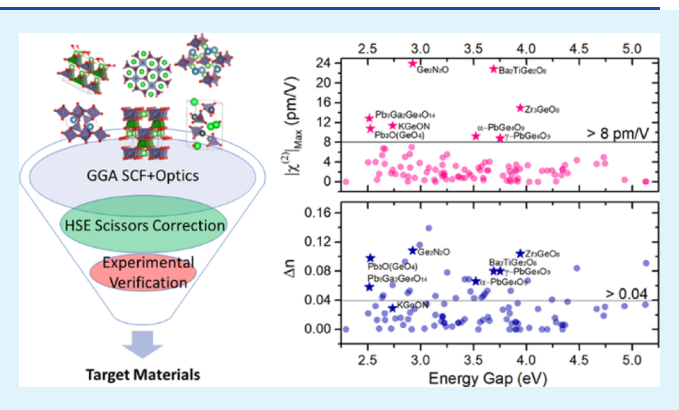
ACCESS

III Metrics & More

Article Recommendations

s Supporting Information

ABSTRACT: Owing to wide infrared (IR) transparency ranges, high laser damage thresholds, and being easy to grow in open air, germanates are emerging as promising mid-infrared (mid-IR) nonlinear optical (NLO) materials. However, the germanates as NLO materials have not been investigated comprehensively and the crystals with large second harmonic generation (SHG) response have not been identified. Herein, we used the first-principles high-throughput screening pipeline for NLO materials to search for excellent NLO crystals from germanates collected in the inorganic crystal structure database. After two steps of screening, three crystals are picked out from 128 structures based on their predicted energy gaps, birefringences, and SHG coefficients. Subsequently, the three germanates are synthesized and measured.



The results show that $Pb_3Ga_2Ge_4O_{14}$ and $Ba_2TiGe_2O_8$ exhibit a wide energy gap (>3.1 eV) and a strong phase-matchable SHG intensity that are comparable to the benchmark $AgGaS_2$ (0.8 and 1.2 × $AgGaS_2$, respectively). In addition, the statistical analyses of different categories classified according to their cations show that the d^0 -transition metal and lone pair cations are more conducive to achieving a larger SHG response and birefringence compared to other cations in germanates. It gives a guideline for exploring new mid-IR NLO materials.

KEYWORDS: nonlinear optical crystals, second harmonic generation, first-principles, high-throughput screening, germanates

1. INTRODUCTION

Coherent sources of mid-infrared (mid-IR) radiation that cover the atmospheric transparent window of 3-5 μ m are widely required in scientific and industrial applications including spectroscopy, explosives detection, free-space communication, and environmental monitoring. ^{1–5} However, the laser sources in this region, especially with high power, are urgently needed. Frequency conversion via nonlinear optical (NLO) materials is a convenient and highly efficient approach to generate mid-IR laser beams. 6-10 Metal chalcogenides are the most primary source of IR NLO materials because of wide transmission ranges in the IR region and large second harmonic generation (SHG) responses. AgGaSe₂, AgGaS₂, and ZnGeP2 represent the benchmark IR NLO materials. Nevertheless, difficulty in crystal growth and especially the low laser damage thresholds (LDTs), which is related to the band gap (E_{σ}) of materials intrinsically, hinder their application in practice. On the contrary, oxides and oxysalts usually exhibit large band gaps and accordingly high LDTs and are easy to grow in open air. However, oxides and oxysalts usually suffer from lower SHG efficiencies. Besides, many of them have narrow optical transmission ranges in the IR region. For example, LiB₃O₅¹² with a transmission range of 0.16–2.6 μ m,

CsLiB₆O₁₀¹³ (0.18–2.7 μ m), β -BaB₂O₄¹⁴ (0.19–3.5 μ m), and KBe₂BO₃F₂¹⁴ (0.155–3.6 μ m) are famous commercial NLO materials that are widely used in the ultraviolet or visible region. Usually, the IR cutoff edge of borates is only around 3 μ m, ¹⁵ which arises from the absorption bands of B–O bonds and their overtones. With the increasing of the atomic mass of the center atoms, the IR cutoff edge extends as well, such as LiNbO₃, ¹⁶ KTiOPO₄ (KTP), ¹⁷ KTiOAsO₄, ¹⁸ and KIO₃. ¹⁹ Unfortunately, each of them shows drawbacks for application in the mid-IR region, such as narrow mid-IR transparency range or low transparency rate. Therefore, searching for mid-IR NLO materials with high LDT, large SHG coefficients, and wide IR transparency is urgent and still a challenge.

Germanates have wide transmission regions that covers the atmospheric transparent window of 3–5 μ m, for example,

Received: September 1, 2020 Accepted: September 14, 2020 Published: September 14, 2020





 $Bi_2Ge_3O_9$ (0.25-6.5 μ m), $Ca_3Ga_2Ge_4O_{14}$ (0.26-6.5 μ m), and $La_3Ga_5GeO_{14}$ (0.24-7.5 μ m). Recently, Xia et al. reported a new titanyl germanate Rb₄Li₂TiOGe₄O₁₂ that exhibits a high LDT about 50 times that of AgGaS2 and a wide transmission range of $0.28-5.58 \mu m$. Subsequently, Yu et al. discovered Li₂K₄(TiO)Ge₄O₁₂ that exhibits a wide transparency range from 0.28 to 5.8 μ m and a high LDT.²² The above two works indicate that germanates are a potential system for searching mid-IR NLO materials. However, both two germanates show a relatively small SHG response of about 2 × KDP at 1064 nm. The germanates that meet the multiple criteria including wide band gaps (>3 eV), large SHG coefficients (>10 × KDP), and sufficient birefringence (>0.04) for phase-matching (PM) are not identified yet. A comprehensive investigation is urgently needed to provide chemical and structural selection guidelines to aid in the search for mid-IR NLO materials with large SHG responses.

Besides discovering new materials, searching NLO materials from reported crystals with determined structures is another approach. However, finding the target materials from existing structures is a time-consuming and high-cost work because of the huge amounts of existing structures and the strict multiple criteria of NLO materials. In order to speed up the progress, many models and theories are proposed to predict the NLO response before crystal growth. Chen et al. had developed a computer-assisted material design system based on anionic group theory.²³ This system has helped them discover famous NLO materials in borates system including LBO (LiB₃O₅), 12 CBO (CsB₃O₅),²⁴ KBBF (KBe₂BO₃F₂),^{14,25} and SBBO (Sr₂Be₂B₂O₇) families.²⁶ Recently, a module-guided design scheme is proposed and proved efficient for NLO materials with target performance.^{27,28} With the development of highperformance computing resources and the improved accuracy of the first principles methods, predicting and screening new functional material based on first-principles approach is receiving increasing attention as a powerful tool to speed up material development.

In this work, we used the first-principles high-throughput screening pipeline for NLO materials (FHSP-NLO) to screen the mid-IR NLO materials from more than 100 germanates. The system could handle large quantities of materials in one go and run automatically. Finally, three germanates are screened out that meet the stringent multiple criteria. Subsequently, three germanates are synthesized. The measurements reveal that Pb₃Ga₂Ge₄O₁₄ and Ba₂TiGe₂O₈ show strong phasematchable SHG intensities that are comparable to that of AgGaS₂ and wider energy gaps than AgGaS₂. Besides, the statistical analyses to different categories classified according to their cations show that the d⁰-transition metal (TM) and lone pair cations play a crucial role in germanates to achieving larger SHG response and birefringence compared to d¹⁰-TM and alkali/alkaline-earth metal cations.

2. METHODS

2.1. FHSP-NLO. The FHSP-NLO method was well described and tested in our recently published paper. The test for well-known NLO crystals and borate systems shows that the method has high accuracy and high efficiency. The noncentrosymmetric (NCS) crystal structures of germanates are downloaded from inorganic crystal structures database (ICSD) (the latest version 4.4.0) by searching the structures that include Ge and O elements. The selected structures are relaxed and the energy gap E_g , birefringence Δn , and SHG coefficients $\chi^{(2)}$ of crystals are predicated from relaxed structures by performing DFT with the generalized gradient approximation (GGA) PBE

(Perdew, Burke, and Ernzerhof)³⁰ exchange—correction functional. The CASTEP package³¹ has been employed to perform self-consistent field and geometry optimization (GO) calculation by using Broyden—Fletcher—Goldfarb—Shanno methods, with the norm-conserving pseudopotentials. The convergence tolerances of GO are set as 1×10^{-5} eV/atom for energy, 0.03 eV/Å for maximum force, 0.05 GPa for maximum stress, and 1×10^{-3} Å for maximum displacement. Tests on reported NLO crystals demonstrate that the above method and computational parameters are sufficiently accurate for present purposes as shown in our previous works. $^{32-40}$ The OptaDOS code $^{41-43}$ is used to calculate linear optical properties by using sum-over-states (SOS) methods. Moreover, the second-order susceptibility $\chi^{(2)}$ tensors are calculated by the formula proposed by Sipe 44 and developed by Lin and Lee et al. 45,46 The structures with an unreasonably small band gap are excluded. Finally, the structures that simultaneously meet the three thresholds ($|\chi^{(2)}_{\rm max}| > 8.0$ pm/V, $\Delta n > 0.04$, and $E_{\rm g}$ -GGA > 1.0 eV) are picked out from all the input structures and sent to the second-round screening.

The hybrid functionals based on screened Heyd-Scuseria-Ernzerhof (HSE) Coulomb potential 47,48 are used to get a more accurate band gap (E_g -HSE) by performing the DFT plane-wave code (PWmat) run on graphics-processing unit machines. 49,50 The scissor operator is set as the difference between E_{σ} -HSE and E_{σ} -GGA and used to correct the SHG coefficients of the crystals that have passed the first-round screening. Then, the crystals that meet the criteria of mid-IR NLO materials are screened out as target materials. To predict birefringence more accurately, the optical permittivity of the selected structures are calculated within the framework of density-functional perturbation theory (DFPT), which is able to respond to an infinitesimal electric field. The refractive indexes and birefringence could be easily calculated from optical permittivity. Subsequently, the powder samples of target materials are synthesized to measure the band gap and SHG response. If experimental measurements are consistent with the predicted results, the single crystal with large size should be grown for comprehensive testing and application evaluation. On the other side, the target materials are used to study the structure-properties relationship by using analysis tools such as partial density of states (PDOS), real-space atom cutting, and the SHG density method. It will further guide the synthesis of new materials with excellent NLO performance.

2.2. Experimental Synthesis and Measurements. 2.2.1. Synthesis. Polycrystalline samples of selected $Ba_2TiGe_2O_8$, $Pb_3Ga_2Ge_4O_{14}$, and $Pb_3O(GeO_4)$ were synthesized by the conventional solid-state method. The initial reagents including $BaCO_3$ (Rhawn, 99.8%), TiO_2 (Aladdin, 99%), PbO (Aladdin, 99.9%), and GeO_2 (hawk, 99.999%) were used without further purification. Stoichiometric amounts of reactants were mixed thoroughly, and heated in a corundum crucible. The samples' purity was confirmed by the powder X-ray diffraction (XRD) study. The reactants, reaction temperature, and time for each compound are listed as below.

2.2.1.1. Ba₂TiGe₂O₈. BaCO₃, TiO₂, and GeO₂ were used. The mixtures were preheated at 1000 °C for 10 h. Then, the temperature was increased to 1050 °C and held for 48 h and then quickly cooled down to room temperature.

2.2.1.2. $Pb_3Ga_2\hat{G}e_4O_{14}$. PbO, Ga_2O_3 , and GeO_2 were used. The mixtures were preheated at 700 °C for 10 h. Then, the temperature was increased to 800 °C and held for 24 h.

2.2.1.3. $Pb_3O(GeO_4)$. PbO and GeO_2 were used. The mixtures were preheated at 650 °C for 10 h. Then, the temperature was increased to 700 °C and held for 24 h.

2.2.2. Powder XRD. Powder XRD patterns of title compounds were collected on a Bruker D8 ADVANCE X-ray diffractometer with Cu $K\alpha$ radiation ($\lambda = 1.5418$ Å) at room temperature. The 2θ range was $10-70^\circ$ with a step size of 0.02° and a fixed counting time of 1 s/step.

2.2.3. UV—Vis—NIR Diffuse-Reflectance Spectra. UV—vis—NIR diffuse reflectance spectra of title samples were collected at room temperature with a SolidSpec-3700DUV spectrophotometer in the wavelength range from 190 to 1100 nm and the reflectance spectra data were converted to absorbance by the Kubelka—Munk transformation.

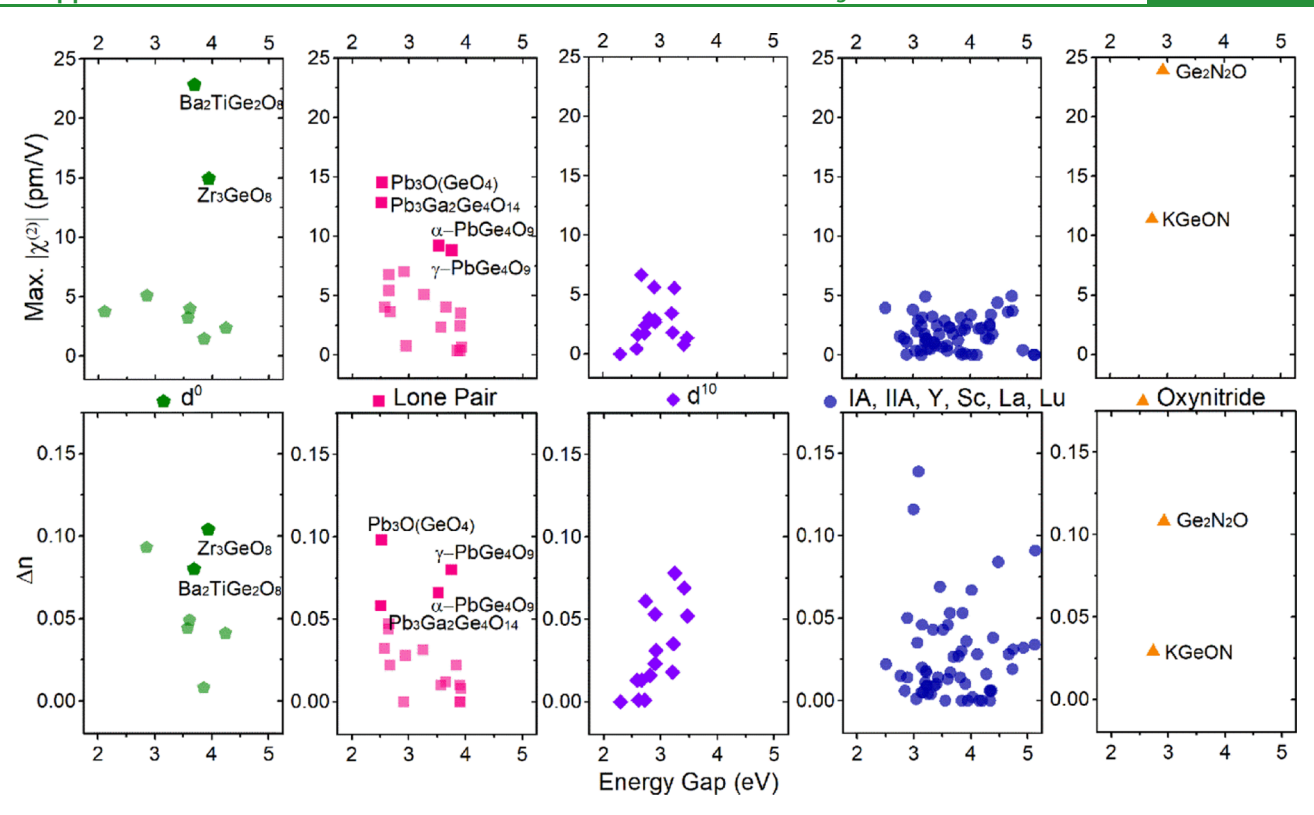


Figure 1. Calculated maximum $\chi^{(2)}$ values and birefringence (Δn) dispersion vs band gap calculated by using GGA functionals of selected germanates that are divided into five categories, that is, geminates containing (i) d^0 -TM cations, (ii) LP activity cations, (iii) d^{10} -TM cations, and (iv) alkali and alkaline-earth metal cations; Y^{3+} , Sc^{3+} , La^{3+} , Lu^{3+} are also included in this category, and the last one is (v) germanium oxynitride.

Table 1. Chemical Formulas, ICSD Collection Numbers, Space Groups (SG), Calculated Band Gaps Both Using GGA and HSE (E_g -GGA and E_g -HSE, Units: eV), Birefringences Calculated by Using the SOS Method at 1064 nm (Δn -SOS), Birefringence Calculated by Using the DFPT Method (Δn -DFTP), and SHG Coefficients ($\chi^{(2)}$) with Scissors Correction of Selected Materials^a

formula	ICSD	SG	E_g -GGA	$E_{\rm g}$ -HSE	Δn -SOS	Δn -DFTP	$\chi(2)$ (pm/V) (+sci.)
$Ba_2TiGe_2O_8$	39133	Cmm2	3.75	5.57	0.080	0.032	$\chi_{113} = -3.32, \chi_{223} = -3.35, \chi_{333} = 10.97$
Zr_3GeO_8	29263	$I\overline{4}2m$	3.90	5.78	0.104	0.065	$\chi_{123} = -6.12$
$Pb_{3}Ga_{2}Ge_{4}O_{14}$	250123	$P3_2$	2.38	3.04	0.058	0.071	$\chi_{112} = -\chi_{222} = -8.83$
$Pb_3O(GeO_4)$	100275	$P2_1$	2.39	3.00	0.098	0.151	$\chi_{112} = -0.63$, $\chi_{123} = 2.56$, $\chi_{222} = -12.86$, $\chi_{233} = -0.0.49$
α -PbGe ₄ O ₉	64910	$P3_2$	3.52	4.49	0.066	0.090	$\chi_{112} = -\chi_{222} = -4.786$
γ -PbGe ₄ O ₉	201282	C2	3.99	4.56	0.080	0.100	$\chi_{112} = 1.76, \chi_{123} = 1.40, \chi_{222} = 4.21, \chi_{233} = -0.19$
Ge_2N_2O	200839	$Cmc2_1$	3.03	4.09	0.108	0.118	$\chi_{113} = -6.16, \chi_{223} = -1.11, \chi_{333} = 14.07$
KGeON	60002	$Pca2_1$	2.91	4.39	0.029	0.130	$\chi_{113} = 0.93, \chi_{223} = 2.20, \chi_{333} = -5.41$
				7-1			

"Note that the scissors operators that are used to correct $\chi^{(2)}$ are set as the difference between $E_{\rm g}$ -HSE and $E_{\rm g}$ -GGA.

2.2.4. Thermal Analysis. Thermal gravimetric (TG) and differential scanning calorimetry (DSC) were carried out on NETZSCH STA 449C instrument at a temperature from room temperature to that above the melting point with a heating rate of 10 $^{\circ}\text{C/min}$ in an atmosphere of flowing N_2 .

2.2.5. SHG Measurement. Through the Kurtz and Perry method, ⁵¹ powder SHG (PSHG) responses of title compounds were investigated by Q-switch laser at both 1064 nm and 2.09 μ m. Polycrystalline samples were ground and sieved into the following particle size ranges: 20–38, 38–55, 55–88, 88–125, 125–160, 160–200, and 200–250 μ m. The sieved KDP and AgGaS₂ samples with the same particle ranges were used as a reference at 1064 nm and 2.09 μ m, respectively. No index-matching oil was used.

3. RESULTS AND DISCUSSION

There are 1990 experimental determined structures that contain Ge and O elements in the ICSD database, in which 519 are NCS. Among the NCS structures, 228 are either solid

solution (alloy) or have atomic positional disorder, 26 structures have unlocated position atoms (mostly are H atoms), 68 structures are determined under high pressures, and all of them are excluded. Besides, 53 structures (Table S1) containing cations with unclosed d or f electronic shell, such as Co²⁺, Cu²⁺, Mn²⁺, Er³⁺, Gd³⁺, Nd³⁺, and Pr³⁺ are also excluded as the d–d or f–f electronic transitions are unfavorable to widen the energy gap. Totally, 144 carefully selected structures are screened by FHSP-NLO. After the calculation, 16 structures (Table S2) are not convergent during the GO step or have unreasonable tiny band gaps. Finally, we got 128 structures that were successfully calculated and analyzed.

To clarify the influence of different cation types to the NLOrelated properties, the successfully calculated structures are catalogued into five sets according to their composition: (i) the structures containing d^0 TM (d^0 -TM) cations (Ti^{4+} , Zr^{4+} , Nb⁵⁺, and Ta⁵⁺), (ii) the structures containing lone-pair (LP) cations (Pb²⁺, Bi³⁺, and Sb³⁺), (iii) the structures containing d¹⁰ TM (d¹⁰-TM) cations (Zn²⁺ and Cd²⁺), (iv) the structures containing alkali, alkaline-earth metal cations, and trivalent rare-earth cations (Sc³⁺, Y³⁺, La³⁺, Lu³⁺). The crystals will be classified to the front set if they contain more than one type of the above cations. The germanium oxynitrides are separated as the (v) category. In addition, the compounds that are not germinated but containing Ge and O atoms are separated and listed in Table S3.

The maximum SHG tensor $|\chi^{(2)}|_{\text{max}}$ and birefringence Δn versus GGA band gap (E_g-GGA) of selected structures calculated by the first-round screening are displayed in Figure 1 as divided into five categories. The detailed information including chemical formula, ICSD number, SG, band gap E_{σ} -GGA, birefringence Δn at 1064 nm, SHG tensors $\chi^{(2)}$ (pm/V) without scissors correction, crystal structural representations, and descriptions are listed and drawn in the Supporting Information. After the first-round calculation, eight crystals are screened out and sent to the second-round screening. Their HSE band gap (E_g -HSE), Δn , and $\chi^{(2)}$ calculated with scissors operator correction are listed in Table 1.

3.1. Germanates Containing d⁰-TM Cations. There are eight NCS crystals (nine structures) that contain d⁰-TM cations with second-order Jahn-Teller effect are investigated including Ba₂TiGe₂O₈, Zr₃GeO₈, RbNbGe₃O₉, ATaGe₃O₉ (A = K, Rb, Tl), K₆Nb₆Ge₄O₂₆, and KTaO(GeO₄). The GeO₄ groups in these structures are isolated (GeO₄)⁴⁻ in Zr₃GeO₈, K₆Nb₆Ge₄O₂₆, and KTaO(GeO₄), polymerized (Ge₂O₇)⁶⁻ dimer in Ba₂Ge₂TiO₈, and (Ge₃O₉)⁶⁻ ring in RbNbGe₃O₉ and ATaGe₃O₉ (A = K, Rb, Tl). TM-O groups are TiO₅ square pyramid, ZrO₈, NbO₆, and TaO₆. The Ge-O groups and the TM-O groups are connected by corner-sharing to form 2D (two-dimensional) layer or 3D (three-dimensional) frameworks. The predicted properties including E_g -GGA, Δn , $\chi^{(2)}$ tensors with structural information are listed in Table S4. Among them, Ba₂Ge₂TiO₈ and Zr₃GeO₈ have large SHG coefficients (>8 pm/V), sufficient birefringence (>0.04), and large band gap (>3.0 eV) during the first-round screening. Both the crystals are analyzed in detail as follows.

3.1.1. Ba₂TiGe₂O₈. Ba₂TiGe₂O₈ crystalizes in polar SG of Cmm2. It features a layered structure, in which the compressed TiO₅ square pyramid connects with the Ge₂O₇ group by sharing four bottom oxygen atoms of TiO5 to form a 2D [TiGe₂O₈]⁴⁻ layer (Figure 2a). The Ba²⁺ cations are located

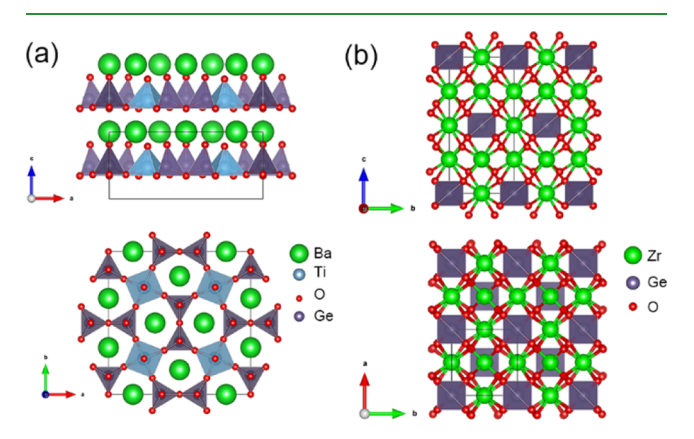


Figure 2. Crystal structures of (a) Ba₂TiGe₂O₈ and (b) Zr₃GeO₈. The GeO₄ and TiO₅ coordination groups are drawn as polyhedra.

between layers to connect the structures and balance the charge. The band structure calculated using GGA (Figure 3a) shows that Ba₂TiGe₂O₈ exhibits an indirect band gap of 3.75 eV. The band gap using HSE functionals is 5.57 eV, which indicates a high LDT. Besides, the birefringence calculated by using the SOS method (\Delta n-SOS) of Ba2TiGe2O8 is 0.080 at 1064 nm (as shown in Figure 3b). However, the birefringence calculated by using the DFPT method (Δn -DFTP) is 0.032, which does not meet the criterion for birefringence. The three independent tensors of Ba₂TiGe₂O₈ calculated with scissor correction are $\chi_{113} = -3.32$, $\chi_{223} = -3.35$, $\chi_{333} = 10.97$ pm/V. According to PDOS (Figure 3c) and SHG density analysis (Figure S1), the occupied O nonbonding 2p orbitals and unoccupied Ti 3d orbitals give the overwhelming contribution to the largest SHG tensor χ_{333} . The consistent orientation of the TiO₅ square pyramid along the c axis results in the large SHG tensor of χ_{333} . The calculated IR vibrational spectrum shows that its highest energy vibration mode is less than 700 cm⁻¹ (Figure 3d).

3.1.2. Zr₃GeO₈. As shown in Figure 2b, Zr₃GeO₈ belongs to the nonpolar SG $\overline{I42m}$ in which the GeO₄ and ZrO₈ groups are connected by sharing O atoms. There are two type of oxygen atoms, in which O(1) is shared by three Zr atoms and O(2) is shared by three Zr and one Ge atoms. All GeO4 units are isolated and toward the same direction. The ZrO₈ units show a tendency of identical orientation. Zr₃GeO₈ shows an indirect band gap of 3.90 eV calculated by using GGA functionals (Figure S2a). The E_g -HSE of Zr_3GeO_8 is 5.78 eV, which is slightly larger than that of Ba₂TiGe₂O₈. As shown in Table 1, the Δn -SOS is 0.104 at 1064 nm (Figure S2b). The Δn -DFPT is 0.065, which is smaller than Δn -SOS, same as Ba₂TiGe₂O₈ but larger than the criterion of 0.04. The only independent SHG tensor with scissor correction χ_{123} is -6.12 pm/V, which is smaller than the criterion of 8.0 pm/V. Combining the PDOS (Figure S2c) and SHG density map (Figure S2e) of Zr₃GeO₈, the occupied O nonbonding 2p orbitals and unoccupied Zr 4d orbitals give the most contribution in both VE and VH processes. It reveals that the ZrO₈ groups are the dominant source of χ_{123} . The near identical orientation of ZrO₈ and GeO4 give rise to relatively large SHG coefficient and birefringence. The calculated highest energy vibration mode is less than 700 cm⁻¹ (Figure S2d).

3.1.3. Others. As shown in Table S4, RbNbGe₃O₉ and $ATaGe_3O_9$ (A = K, Rb, Tl) are isostructural and crystallize in a hexagonal crystal system with SG of P6c2. Three GeO₄ groups are linked to form a six-membered Ge₃O₉ ring. Ta (or Nb) is octahedrally coordinated by six terminal O atoms from six different Ge₃O₉ rings. Alkali metal cations are located in the tunnels of the framework constructed by the Ge₃O₉ rings and $Ta(Nb)O_6$ octahedra. $RbNbGe_3O_9$ shows a smaller E_σ -GGA (2.85 eV) than those of ATaGe₃O₉ (A = K, Rb, Tl) (\sim 3.6 eV) and accordingly a larger SHG coefficient ($\chi_{122} = 5.056 \text{ pm/V}$) and birefringence (0.093) than the latter. K₃Nb₃Ge₂O₁₃ crystallizes in the SG of $P\overline{6}2m$, in which the NbO₆ octahedral is connected with each other constructing triple chains along the c axis that are further connected by the GeO₄ groups to build up a 3D framework. E_g-GGA of K₃Nb₃Ge₂O₁₃ is much smaller (2.11 eV) than those of other d⁰-TM germanates but has a very large birefringence of 0.306 and a moderate SHG coefficient $\chi_{222} = 3.71$ pm/V. In KTaO(GeO₄), the TaO₆ octahedra are linked by the GeO₄ groups to form a 3D framework. The K cations are located in the channels of the frameworks. It has a large E_g -GGA of 4.24 eV and a moderate

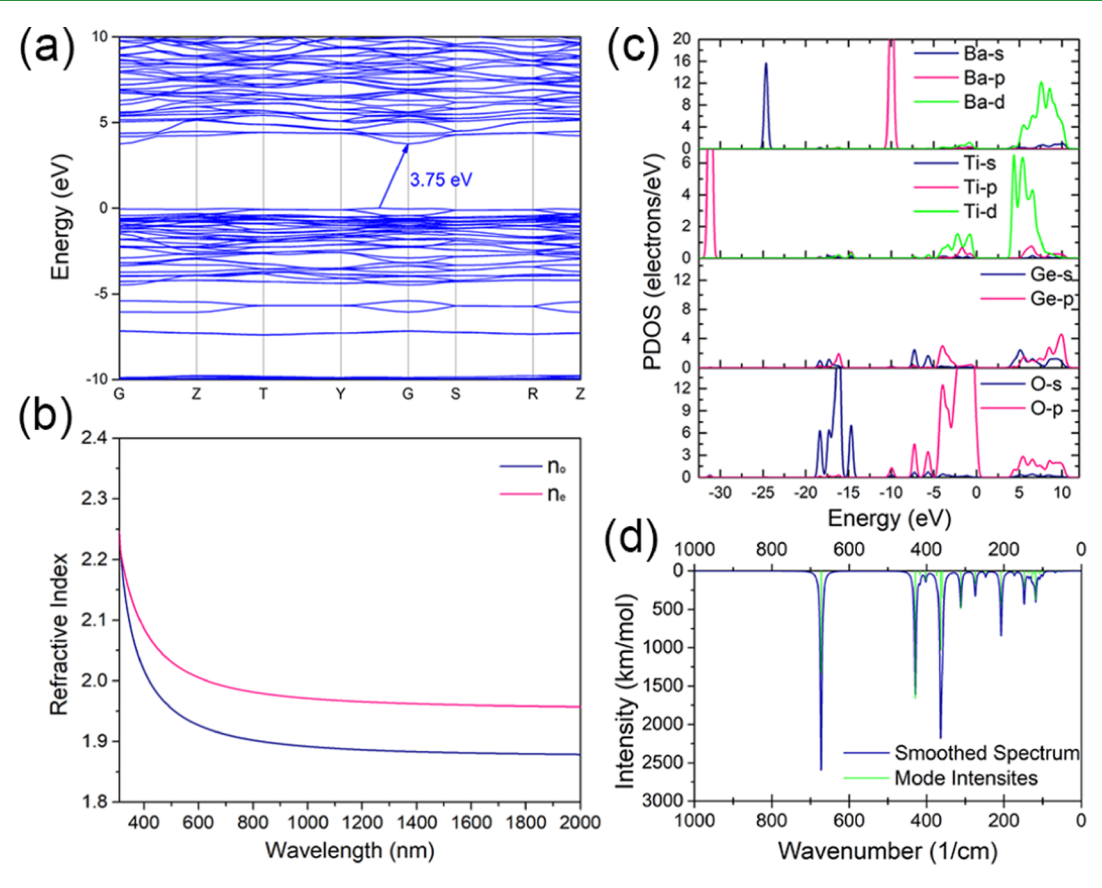


Figure 3. (a) Band structure, (b) refractive index with the shortest PM wavelength (n_x and n_y are very closed and overlapped), (c) PDOS, and (d) IR vibrational spectrum of Ba₂TiGe₂O₈.

birefringence of 0.041. The maximum SHG tensor χ_{333} is 2.31 pm/V. All the above six d⁰-TM germanates have not met the criteria of SHG coefficients.

3.2. Germanates Containing LP Cations. Seventeen germanates (23 structures) with NCS crystal structures containing LP cations of Pb2+, Bi3+, and Sb3+ are investigated including Pb₃Ga₂Ge₄O₁₄, Pb₃O(GeO₄), PbGe₄O₉ (P3₂), PbGe₄O₉ (C2), Bi₁₂GeO₂₀, Bi₂GeO₅ (Cmc2₁), Bi₂GeO₅ (Cc), $PbSrGeO_4$, $PbBaGeO_4$, $Pb_5Ge_3O_{11}$ ($P\overline{6}$), $Pb_5Ge_3O_{11}$ (P3), $A_4(GeO_4)_3(A = Sb, Bi)$, PbGeTeO₆, and ASbO(GeO₄)(A = Na, K, Rb). Two distinctive coordination environments of Ge atoms exist in this category germanates, that is, the GeO4 tetrahedron and the GeO₆ octahedron. The connection patterns of Ge-O display abundant structural diversities including isolated GeO₄ or GeO₆, chains constructed by GeO₄ or by both GeO₄ and GeO₆, and the 3D framework constructed by GeO₄ and GeO₆. The detailed information including predicted properties with crystal structural representations and descriptions are listed in Table S5. Among them, Pb₃Ga₂Ge₄O₁₄, Pb₃O(GeO₄), α-PbGe₄O₉, and γ-PbGe₄O₉ are screened out via the first-round screening with large SHG coefficients (>8 pm/V), sufficient birefringence (>0.04), and large band gap (>3.0 eV) and analyzed in detail as follows. Pb₃Ga₂Ge₄O₁₄ and Pb₃O(GeO₄) pass through the second-round screening.

3.2.1. $Pb_3Ga_2Ge_4O_{14}$. $Pb_3Ga_2Ge_4O_{14}$ is a langasite-type compound and crystallizes in the $P3_2$ SG with a uniaxial symmetry. In $Pb_3Ga_2Ge_4O_{14}$, GeO_4 and GeO_6 are connected with each other by corner-sharing at a ratio of 3:1, forming irregular $[Ge_4O_{12}]^{8-}$ chains along the c axis. The GaO_4 tetrahedra further link these chains to construct a 3D

framework with the Pb²⁺ cations located in the channels (Figure 4a). It shows an indirect band gap. $E_{\rm g}$ -GGA and $E_{\rm g}$ -HSE are 2.38 eV (Figure 5a) and 3.04 eV, respectively. The ascalculated birefringence is 0.058 at 1064 nm (Figure 5b). The scissor of 0.66 eV is used to correct the calculation of $\chi^{(2)}$.

The SHG tensor of $Pb_3Ga_2Ge_4O_{14}$ is $\chi_{112} = -\chi_{222} = -8.83$ pm/V. The calculated IR vibrational spectrum shows that its highest energy vibration mode is less than 800 cm⁻¹ (Figure 5d). The SHG density (Figure S3) and PDOS (Figure 5c) reveal that the larger coefficients mainly originate from O and Pb atoms. It is interesting that $Ba_3Ga_2Ge_4O_{14}$ is isostructural with $Pb_3Ga_2Ge_4O_{14}$ but its SHG coefficient without scissor correction and birefringence ($\chi_{222} = 3.949$ pm/V; $\Delta n = 0.022$) is much smaller than that of $Pb_3Ga_2Ge_4O_{14}$ ($\chi_{222} = 12.832$ pm/V; $\Delta n = 0.058$). This comparison indicates that the Pb^{2+} cations with LP electrons give the main contribution to both SHG and birefringence in $Pb_3Ga_2Ge_4O_{14}$.

3.2.2. $Pb_3O(GeO_4)$. $Pb_3O(GeO_4)$ belongs to the $P2_1$ SG in which the connection of Ge–O forms solely isolated GeO_4 tetrahedron. Besides, one-fifth oxygen atoms in the cell are not bonded with Ge but are surrounded by six Pb atoms (Figure 4b). $Pb_3O(GeO_4)$ is predicted to have a direct band gap (Figure S4a). The E_g -GGA and E_g -HSE are 2.39 and 3.00 eV, respectively. A scissors operator of 0.61 eV is used to correct $\chi^{(2)}$. The results show that $Pb_3O(GeO_4)$ exhibits a lager SHG coefficient ($\chi_{222} = -12.86$ pm/V) and appropriate birefringence of 0.098 at 1064 nm (Figure S4b). The highest energy IR vibration mode is less than 750 cm⁻¹ (Figure S4d). The coordination environment around the Pb atoms indicates that it exhibits stereochemical activity. It is also confirmed by the LP electronic characteristics that the s orbitals of Pb appear at

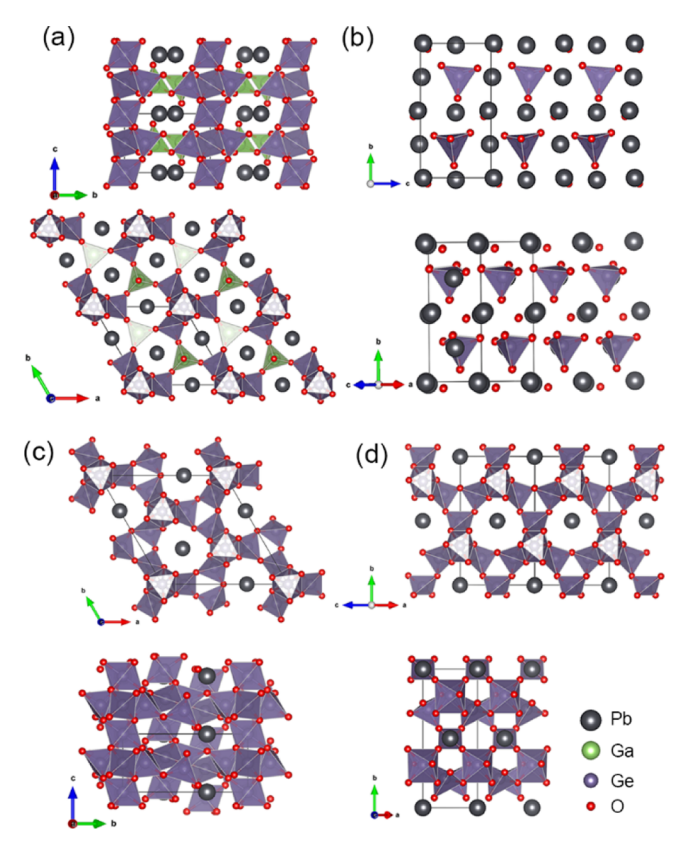


Figure 4. Crystal structures of (a) $Pb_3Ga_2Ge_4O_{14}$, (b) $Pb_3O(GeO_4)$, (c) α- $PbGe_4O_9$, and (d) γ- $PbGe_4O_9$. The GeO_4 , GeO_6 , and GaO_4 coordination groups are drawn as polyhedra.

the top of the upper valence band as shown in PDOS (Figure S4c). The SHG density map (Figure S4e) combined with PDOS of $Pb_3O(GeO_4)$ reveal that the largest SHG coefficient χ_{222} mainly originates from O atoms and Pb atoms. It is worth noting that the determined structure of $Pb_3O(GeO_4)$ may have some problems and will be discussed in Section 4.

3.2.3. PbGe₄O₉. There are two NCS phases among the four structures of PbGe₄O₉. α -PbGe₄O₉ and γ -PbGe₄O₉ crystallize in the P32 and C2 SG, respectively. The basic building units (BBUs) and connection pattern are same in the two phases, in which GeO₄ tetrahedra and GeO₆ octahedra are connected forming irregular [Ge₄O₁₂]⁸⁻ chains which are same as that in Pb₃Ga₂Ge₄O₁₄. The chains are further polymerized to form a 3D skeleton with channels in which the Pb atoms are located (Figure 4c,d). The electronic structure of γ-PbGe₄O₉ was calculated in detail and analyzed as shown in Figure S5. α -PbGe₄O₉ and γ-PbGe₄O₉ exhibit large band gaps of 3.52 and 3.99 eV, respectively, calculated by using the GGA functional. The predicted $E_{\rm g}$ -HSE are 4.49 and 4.56 eV for the α and γ phases, respectively. Both phases show larger birefringence of 0.066 and 0.080 at 1064 nm. Unfortunately, the largest SHG tensors are too small ($\chi_{222} = 4.786$ pm/V and $\chi_{222} = 4.21$ pm/V, respectively) to meet the criterion. The Pb²⁺ cations also show a stereochemical active LP effect. The PDOS and SHG density map of γ -Pb₃O(GeO₄) reveal that O and Pb atoms are the main resource of the largest SHG coefficient as shown in Figure S5. The calculated IR vibrational spectrum shows that its highest energy vibration mode is less than 950 cm⁻¹. It is worth to note that α-PbGe₄O₉ is isostructural with BaGe₄O₉ and SrGe₄O₉. However, the SHG coefficients and birefringence calculated without scissors correction of BaGe₄O₉ and

SrGe₄O₉ ($\chi_{222} \approx 1.0 \text{ pm/V}$; $\Delta n \approx 0.01$) are much smaller than that of α-PbGe₄O₉ ($\chi_{222} = 9.199 \text{ pm/V}$; $\Delta n = 0.066$) although they have similar band gaps. This case further reveals that the Pb²⁺ cations are the key factor for large SHG and birefringence in α-PbGe₄O₉.

3.2.4. Others. In Bi₁₂GeO₂₀ and Bi₂GeO₅, the Bi cations are coordinated with O, forming BiO₅ pyramids that show strong stereochemical active LP effect (Table S5). In Bi₁₂GeO₂₀, the Ge atoms form isolated GeO₄ groups. The predicted SHG coefficient χ_{123} is about 7 pm/V calculated from three structures collected in independent works. Unfortunately, Bi₁₂GeO₂₀ belongs to a cubic crystal system and its birefringence is 0 and cannot achieve PM. Bi₂GeO₅ is constructed by (GeO₃)²⁻ chains and (Bi₂O₂)²⁺ sheets that built up with basal edge-shared BiO₅ pyramids. Two NCS SGs, that is, Cmc21 and Cc, are determined for Bi2GeO5. The detailed comparison shows that the two structures are very similar. As a result, the calculated properties for these two structures are also very close. As shown in Table S5, the calculated band gaps of two SGs are about 2.6 eV, a moderate birefringence of about 0.045, and a large SHG coefficient of χ_{113} around 6 pm/V. PbSrGeO₄ and PbBaGeO₄ are isostructural where the isolated GeO4 groups are separated by Pb and Sr (Ba) cations. The two crystals show a similar and relatively large band gap of about 3.6 eV but a very small birefringence of 0.01. The only independent SHG coefficient χ_{123} of PbSrGeO₄ and PbBaGeO₄ are 4.05 and 2.35 pm/V, respectively. Similar to Bi₂GeO₅, Pb₅Ge₃O₁₁ was found in two different NCS SGs, that is, ferroelectric phase trigonal P3 and paraelectric phase hexagonal $P\overline{6}$. Both of the structures consist of GeO₄ tetrahedra and Ge₂O₇ double tetrahedra. Two phases exhibit a similar band gap of about 2.6 eV, which is slightly different, but a small birefringence of 0.033 and 0.022 as well as moderate SHG coefficients of around 4 pm/V. Sb₄(GeO₄)₃ and Bi₄(GeO₄)₃ are isostructural and belong to cubic crystal symmetry with the $I\overline{4}3d$ SG. Therefore, the birefringence is 0 although they show a large band gap of about $3.9\ eV$ and SHG tensor of around 3 pm/V. PbGeTeO₆ crystallizes in the SG of P32 and consists of (GeTeO₆)²⁻ sheets composed by edgesharing of GeO₆ and TeO₆ octahedra, Pb²⁺ cations located between the sheets. It shows a band gap of 2.94 eV, a birefringence of 0.028 at 1064 nm, and SHG coefficient of χ_{122} = 0.80 pm/V. CdGeTeO₆ and SrGeTeO₆ are isostructural with PbGeTeO₆. Among them, SrGeTeO₆ has the largest band gap of 3.6 eV and CdGeTeO₆ keeps the largest birefringence of 0.061 and largest SHG coefficient of χ_{122} = 2.404 pm/V. It is worth noting that PbGeTeO6 has the smallest birefringence and SHG coefficient. This case is opposite to other cases, such as $A_3^{II}Ga_2Ge_4O_{14}$ ($A^{II} = Pb$ or Ba) and $A^{II}Ge_4O_9$ ($A^{II} = Pb$, Ba, Sr), in which the Pb-containing structure exhibits the much higher SHG coefficients and birefringence compared to their counterparts. It means that not all substitutions of Pb²⁺ could enhance SHG properties. ASbOGeO₄ (A = Na, K, Rb) are another class with same structures belonging to the Pna21 SG in which SbO₆ octahedra and GeO₄ tetrahedra are connected by corner-sharing to construct an irregular 3D framework; the alkali metal cations are located in the framework. The band gaps of this class are about 3.8 eV, but the birefringence and SHG coefficients are very small.

3.3. d¹⁰-Metal Germanates. Fourteen crystals (18 structures) containing d¹⁰-metal cations (Zn^{2+} and Cd^{2+}) are investigated in this section including Na_2ZnGeO_4 , Li_2ZnGeO_4 , Li_2CdGeO_4 , $Ca_3ZnGe_5O_{14}$, $La_3SbZn_3Ge_2O_{14}$, $Ca_2Zn(Ge_2O_7)$,

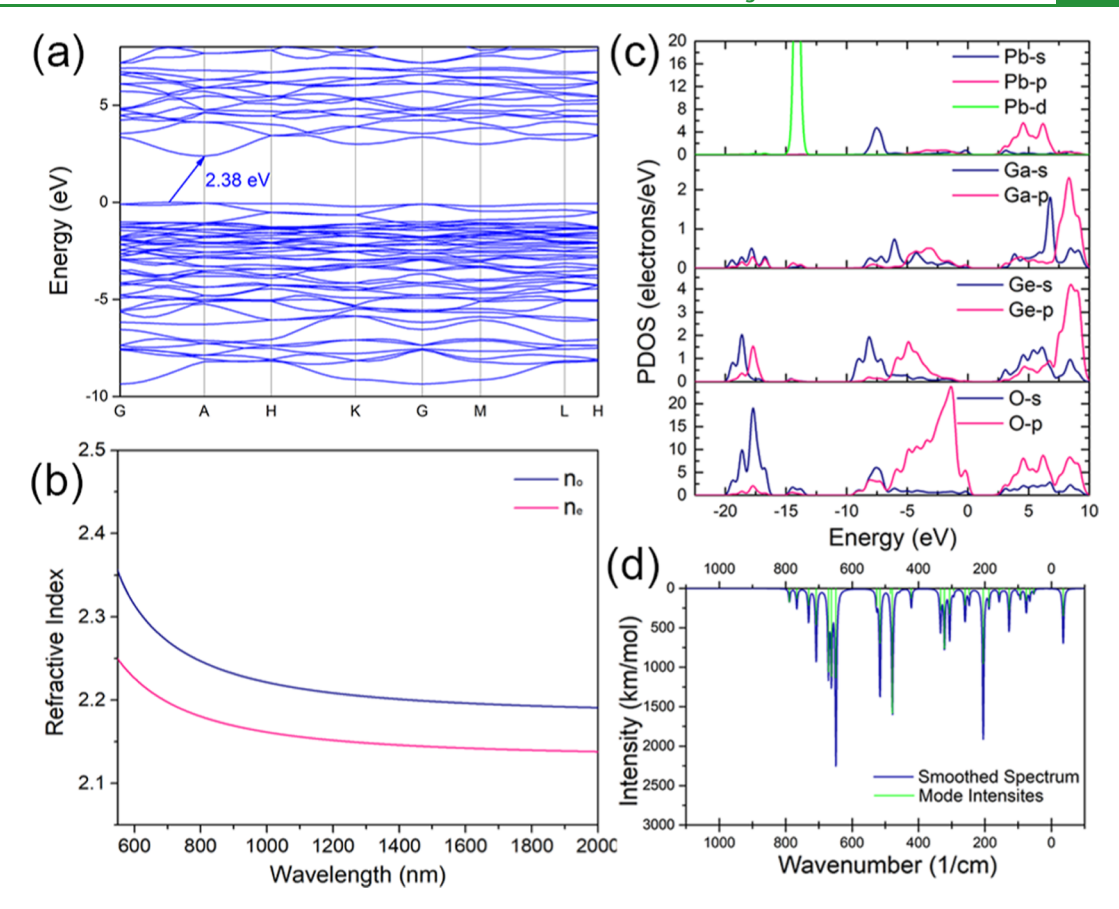


Figure 5. (a) Band structure, (b) refractive index with the shortest PM wavelength, (c) PDOS, and (d) IR vibrational spectrum of Pb₃Ga₂Ge₄O₁₄.

 $Ba_2ZnGe_2O_7,\ Sr_2ZnGe_2O_7,\ K_2ZnGe_2O_6,\ K_2Zn(GeO_4),\ CdGeTeO_6,\ Cd_2Ge_7O_{16},\ Cd_{12}B_8Ge_{17}O_{58},\ and\ Zn_2Ge_3O_8.$ These crystals demonstrate the rich structural diversity by multiple coordination types of Ge and Zn (GeO_4, GeO_6, ZnO_4, and ZnO_6) with different connection modes between them. The predicted properties with their structural information are listed in Table S6. Among them, no material strictly meets the criteria for mid-IR materials. However, some materials are close to the criteria including $Ca_3ZnGe_5O_{14}$ and $La_3SbZn_3Ge_2O_{14}.$ The detailed analyses are described as follows.

Ca₃ZnGe₅O₁₄ and La₃SbZn₃Ge₂O₁₄ are isostructural and belong to the C2 SG. The two crystals have the same structural configuration as Pb₃Ga₂Ge₄O₁₄ but a low symmetry. The predicted band gap and birefringence (Ca₃ZnGe₅O₁₄: 2.89 eV, 0.053; La₃SbZn₃Ge₂O₁₄: 3.25 eV, 0.078) meet the criteria but the largest SHG coefficients ($Ca_3ZnGe_5O_{14}$: $\chi_{222} = 5.620$ pm/ V; La₃SbZn₃Ge₂O₁₄: $\chi_{233} = 5.554$ pm/V) are relatively small. The small SHG of these two materials compared with Pb₃Ga₂Ge₄O₁₄ can be attributed to the Ca²⁺ and La³⁺ cations that have a negligible contribution for SHG response compared to that of Pb²⁺. Na₂ZnGeO₄ and Li₂ZnGeO₄ belong to the Pn SG and are isostructural. They have a structure similar to Li₂CdGeO₄ (Pmn2₁), in which GeO₄, ZnO₄ (CdO₄) and LiO₄ (NaO₄) tetrahedra with the roughly same orientation are connected with each other by corner-sharing to build up a regular 3D framework. Li₂ZnGeO₄ has a larger band gap (3.21 eV) than Na₂ZnGeO₄ (2.67 eV) and as a consequence a smaller SHG coefficient (χ_{333} = 3.44 pm/V) than that of Na₂ZnGeO₄ (χ_{333} = 6.66 pm/V). Li₂CdGeO₄ shows a band gap of 2.90 eV and a small χ_{113} of -2.885 pm/V. All the three

structures exhibit a very small birefringence (0.013–0.023). Ba₂ZnGe₂O₇, Sr₂ZnGe₂O₇, and Ca₂ZnGe₂O₇ are another type of structures that have the same structure belonging to the $P\bar{4}2_1m$ SG where Ge₂O₇ double tetrahedra and ZnO₄ build up [ZnGe₂O₇]^{4–} layers separated by Ba/Sr/Ca cations, respectively. The predicted SHG coefficients are very small despite their large band gap and moderate birefringence.

As described in the reference, 54 K₂Zn(Ge₂O₆) is built up of the ZnO_4 and GeO_4 tetrahedra by corner-sharing, forming the framework with Zn^{2+} located in the interspace. However, the coordination of Zn is unreasonable ZnO2 according to crystallographic data in ref 54 as well as CIF file (ICSD: 65740). We guess that there are some mistakes in positional parameters of K₂Zn(Ge₂O₆) reported in the paper and CIF file. However, what is exciting is that the optimized structure becomes reasonable and is consistent with the description in the paper. This case demonstrates that GO is necessary for the high-throughput screening to correct the structures with some local inaccuracy, especially for the structures collected in the early stage. The band gap, birefringence, and SHG coefficients calculated based on the optimized structure of $K_2Zn(Ge_2O_6)$ are 2.81 eV, 0.016, and $\chi_{123} = -3.027$ pm/V, respectively. In K₂ZnGeO₄, the ZnO₄ and GeO₄ tetrahedra are linked by corner-sharing to construct a 3D network with the K+ cations filled in. $Cd_{2}Ge_{7}O_{16}$ and $Cd_{12}B_{8}Ge_{17}O_{58}$ contain the same [Ge₄O₁₂]⁸⁻ chains composed by GeO₆ and GeO₄, same as in Pb₃Ga₂Ge₄O₁₄. All the above three crystals display a small SHG coefficient (<2.0 pm/V) and birefringence (<0.013). Zn₂Ge₃O₈ constructed by ZnO₄ and GeO₆ belonging to the cubic crystal system with P4332 SG. Therefore, as we calculated, its birefringence and SHG coefficients are 0.

3.4. Alkali and Alkaline-Earth Metal Germanates. The germanates that contain alkali and/or alkaline-earth metal are studied in this section. Besides, trivalent rare-earth ions (Sc³⁺, Y³⁺, La³⁺, Lu³⁺) are also included in this section because these ions have closed-shell electronic configuration and avoid the d-d or f-f electronic transition and broaden transparent region, just like the behavior of alkali and alkaline-earth metal ions. A total of 58 germanates (65 structures) are investigated including LiB(GeO₄)($\overline{I4}$), LiB(GeO₄)(Fmm2), Li₂Ge₂O₅, La(BGeO₅), Ba₃Ga₂Ge₄O₁₄, CsGeB₃O₇, RbGeB₃O₇, Li_2CaGeO_4 , $La_2Ge_2O_7$, $Li_4Ge_9O_{20}$, $Li_8O_2(GeO_4)$, $Li_2(GeO_3)$, Na₂(GeO₃), NaKGeO₃, SrGeO₃, Li₈(AlGeO₄)₆I₂, $Li_8(AlGeO_4)_6Br_2$, $Li_8(AlGeO_4)_6Cl_2$, $Na_8(Al_6Ge_6O_{24})Cl_2$, $Na_8(Al_6Ge_6O_{24})Br_2$, $Na_8(AlGeO_4)_6I_2$, $Sr(GeTeO_6)$, $Li_3(GaGeO_5)$, $Li_3(AlGeO_5)$, $Na(Ge_4(PO_4)_3)$, $K(BGe_2O_6)$, $Ba(GeO_3)$, $K_2(B_2Ge_3O_{10})$, $Sr(H_2GeO_4)$, $RbGe(IO_6)$, $K_4BaGe_3O_9$, $Rb_4Ge_3B_6O_{17}$, $K_6(Ge_2O_7)$, $LiAlGeO_4$, $Na_4K_2(Ge_2O_7)$, $Ca_2Ge_7O_{16}$ (Pba2 and $P\overline{4}b2$), $Li_2Ge_7O_{15}$, $K_6(Ge_2O_7)$, $Ba(Ge_4O_9)$, $Sr(Ge_4O_9)$, $KGeOPO_4$, $Na_4Sc_2(Ge_4O_{13})$, $BaSnGe_3O_9$, $Ca_{12}Ge_{17}B_8O_{58}$, $La_2Ge(Be_2O_7)$, $Y_2Ge(Be_2O_7)$, $Ba_2Mg(Ge_2O_7)$, $Sr_2Mg(Ge_2O_7)$, $Li_2Ge_4O_9$, $LiNa(Ge_4O_9)$, $Sr_2(GeO_4)$, $NaY(GeO_4)$, $CaGe_2O_5$, La₂MgGeO₆, Mg₁₀(Ge₃O₁₄(OH)₄), Lu₂(Ge₂O₇), and $Y_2(Ge_2O_7)$. The germanates in this classification show plentiful structural diversity including (i) 0D isolated GeO₄ tetrahedron, Ge₂O₇ double tetrahedra, Ge₃O₁₀ ring, and GeO₆ octahedron; (ii) 1D Ge₃O₁₀ short chain, infinite [GeO₃] chain, and infinite [BGeO₅] spiral chains consisting of BO₄ and GeO₄; (iii) 2D layers built by GeO₄ and BO₄ or GeO₆ and IO₆, (iv) 3D frameworks made up of BBUs chosen from GeO₄, GeO₆, GeO₃ pyramid, BO₄, PO₄, AlO₄, GaO₄, and SnO₆. The predicted properties with their structural information are listed in Table

All the 56 germanates in this category show relatively small SHG coefficients (<5 pm/V, as shown in Table S7) but abundant and diverse structures. Among them, LiB(GeO₄) with the $\overline{I4}$ SG has the largest SHG coefficient ($\chi_{123} = 4.962$ pm/V), followed by $\text{Li}_2\text{Ge}_2\text{O}_5$ ($\chi_{113} = 7.927 \text{ pm/V}$) and $La(BGeO_5)$ ($\chi_{333} = -4.408 \text{ pm/V}$). $Ba_3Ga_2Ge_4O_{14}$ was discussed together with Pb₃Ga₂Ge₄O₁₄ in the above section. The case also reveals the reason why alkali and/or alkalineearth metal germanates exhibit relatively small SHG tensors compared to germanates containing LP cations or d⁰-metals. As to birefringence, a dozen of them meet the criteria (>0.04) and some show a very larger value, such as SrGeO₃ ($\Delta n =$ 0.139) and Li(BGeO₄) with the Fmm2 SG ($\Delta n = 0.116$). It is worth to note that the description of Li(BGeO₄) with Fmm2 SG was proved to be wrong and its real symmetry at room temperature is $\overline{14}$. So $\overline{55}$ Unfortunately, the real structure exhibits a very small birefringence but large SHG coefficients and band gap. 58,59 Considering multiple criteria including band gap, birefringence, and SHG response, $La_2Ge_2O_7$ ($E_g = 4.366$ eV, $\Delta n = 0.067$, $\chi_{222} = 3.351$ pm/V) is the best candidate but with a relatively small SHG coefficient. In addition, La-(BGeO₅) ($E_g = 4.478 \text{ eV}$, $\Delta n = 0.084$, $\chi_{113} = 4.408 \text{ pm/V}$) is expected to be used in visible and UV regions where the criterion for SHG is relatively low but not the IR region because of the absorption aroused by the BO₄ group. More accuracy prediction and experimental study for La₂Ge₂O₇ and Li(BGeO₄) are necessary, but they are out of the topic of this

3.5. Germanium Oxynitride. During the searching of germanates, two germanium oxynitride, that is, Ge₂N₂O and

KGeON, came into our sight although they are not defined germanates. Interestingly, both materials show very wide band gaps, remarkable birefringence, and large SHG coefficients in the first-round screening as shown in Table S8.

3.5.1. Ge_2N_2O . The crystal structure of Ge_2N_2O is orthorhombic ($Cmc2_1$) and is isostructural with Si_2N_2O . The structure consists of the distorted GeN_3O tetrahedra linked with their corner by N atoms in the bc plane and O atoms along the a axis and forming a α -quartz-like structure. Ge and N atoms reside in puckered hexagonal 2D layers, which are further linked by Ge-O-Ge bonds (Figure 6a). Ge_2N_2O

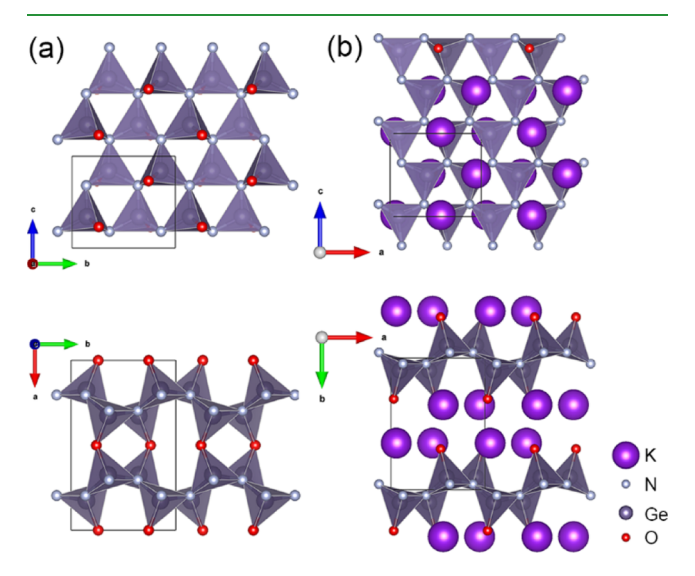
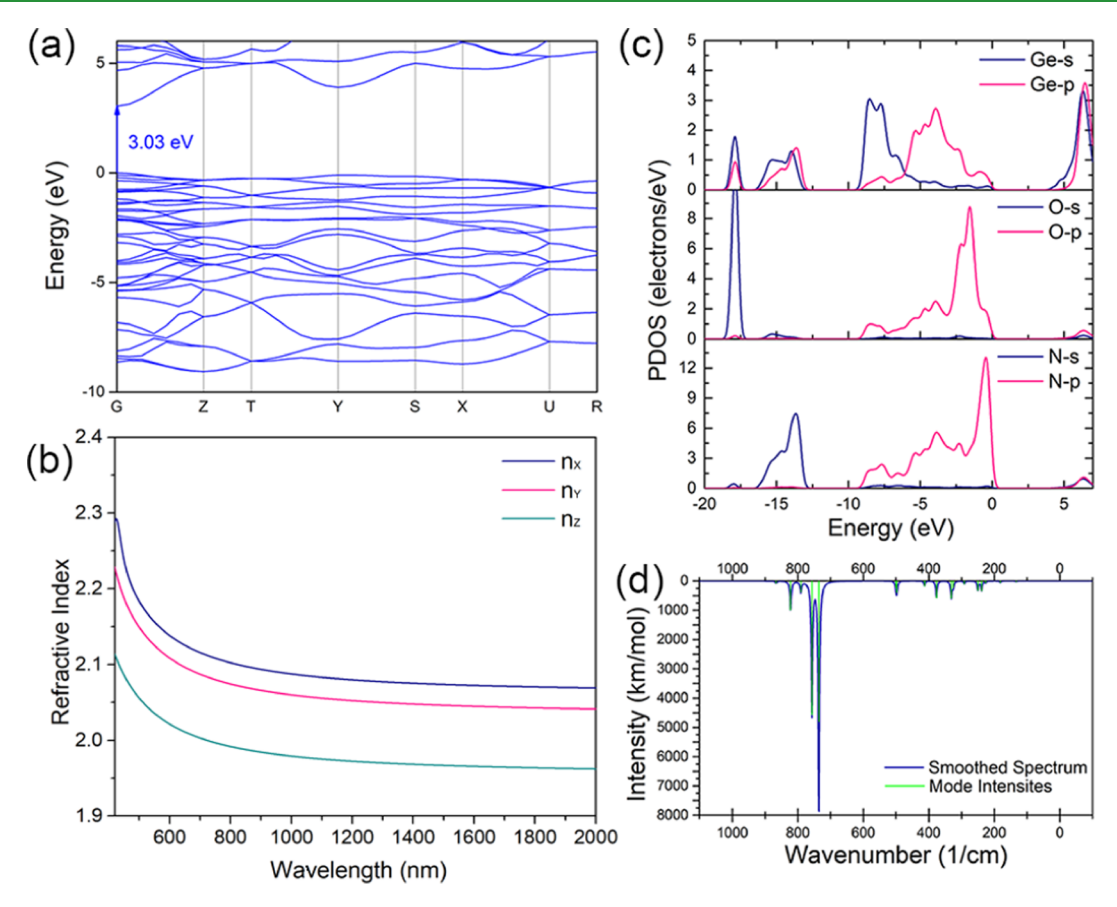


Figure 6. Crystal structures of Ge_2N_2O and KGeON. The $GeON_3$ groups are drawn as tetrahedra.

shows an indirect band gap $E_{\rm g}$ -GGA of 3.03 eV (Figure 7a). The predicted $E_{\rm g}$ -HSE, birefringence, and scissors-corrected SHG coefficient are 4.09 eV, 0.108, and $\chi_{333}=14.07$ pm/V, respectively (Figure 7b). Most importantly, its highest energy IR mode is down to 870 cm⁻¹, similar to that of germanates (Figure 7d). It means that Ge_2N_2O is transparent in the mid-IR region. The PDOS (Figure 7c) and SHG density (Figure S6) reveal that the occupied nonbonding 2p orbital of N and O atoms and unoccupied orbital of Ge, N, and O atoms give the main contribution to χ_{333} .

3.5.2. KGeON. The structure of KGeON can be described as the K⁺ cations inserted into Ge_2N_2O in which each O atom is split into two and the network cleave to $[Ge_2O_2N_2]^{2^-}$ layers (Figure 6b). The introduction of K⁺ has no significant effect on the band gap and highest energy IR mode but significantly reduces SHG coefficients as shown in Table 1 and Figure S7. The Δn -DFTP is 0.130, much larger than the value calculated by using the SOS method.

3.6. Other Crystals Containing Ge and O. The NCS crystals that contain Ge and O atoms but not germanates are also calculated by the first-round screening and listed in Table S3. Among them, $Co(CO)_4GeCl_3$, $Ru(CO)_4(GeCl_3)_2$, and ClO_2GeF_5 show very larger SHG coefficients (>10 pm/V). However, the CO and ClO_2 anionic units would induce vibrational absorption in the mid-IR region. $Ba_2ZnGe_2S_6O$ and $Sr_2ZnGe_2S_6O$ exhibit large birefringence and SHG coefficients. However, they cannot be grown in open air and lose the advantage of germanates. $Na_4(GeSe_4)(H_2O)_{14}$ has a problem similar to $Ba_2ZnGe_2S_6O$. The SHG coefficients of $Na_2(GeSe_4)$



www.acsami.org

Figure 7. (a) Band structure, (b) refractive index with the shortest PM wavelength, (c) PDOS, and (d) IR vibrational spectrum of Ge₂N₂O.

 $(S_2O_7)_3$) and Ba $(Ge(S_2O_7)_3)$ are too small. $Ge(CH_3SO_3)_2$ belongs to the $P4_12_12$ SG and has no nonzero SHG coefficient restricted by symmetry.

Through the systematically classification and investigation, we find that the cations play an important role for SHG response and birefringence. As shown in Figure 1, the crystals that meet the criteria for mid-IR NLO materials are concentrated in the d⁰-TM and LP categories. To make an overall comparison among them, the statistical average values of $E_{\rm g}$ -GGA, $|\chi^{(2)}|_{\rm max}$, and Δn for each category with different cation types are calculated and drawn in Figure 8. One can

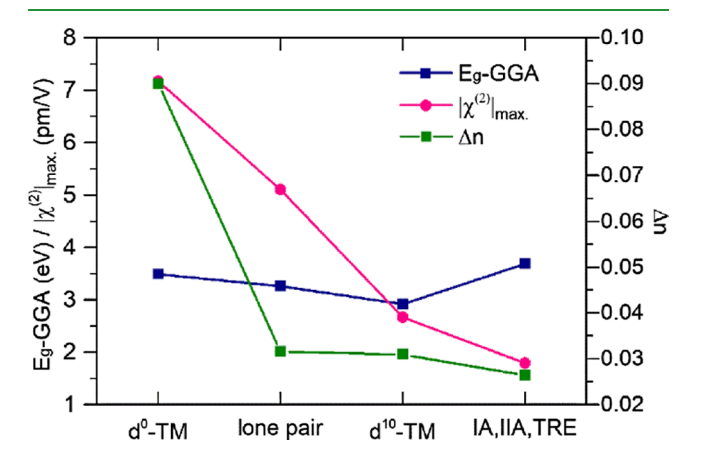


Figure 8. Statistical average values of band gap ($E_{\rm g}$ -GGA), maximum SHG tensor ($|\chi^{(2)}|_{\rm max}$), and birefringence (Δn) of germanates that contain d⁰-TM cations, LP cations, d¹⁰-TM cations, alkali, alkalineearth metal cations, and trivalent rare-earth cations (IA, IIA, TRE).

easily find that the average $|\chi^{(2)}|_{max}$ almost linearly decreases with the cations from d⁰-TM (7.17 pm/V) to LP (5.11 pm/V) to d¹⁰-TM (2.67 pm/V), and to alkali/alkaline-earth/trivalent rare-earth (IA/IIA/TRE, 1.79 pm/V). It means that the contribution for SHG is d^0 -TM > LP > d^{10} -TM > IA/IIA/ TRE. In other words, it has a high probability to find germanates having large $\chi^{(2)}$ at the front in the above ranking. However, it does not mean that d⁰-TM germanates always have larger SHG response than those with LP and others. The final values depend on their composition and structural characteristics. The average birefringences have a tendency similar to $|\chi^{(2)}|_{\text{max}}$. IA/IIA/TRE germanates show the largest average band gap (3.70 eV) as expected. Indeed, the average band gaps of d⁰-TM (3.49 eV) and LP germanates (3.25 eV) are not much smaller than those of IA/IIA/TRE germanates and meet the criterion of 3.0 eV. In conclusion, d⁰-TM and LP germanates are the preferred systems for exploring new mid-IR NLO materials.

4. EXPERIMENTAL VERIFICATION

Three target materials, that is, $Pb_3Ga_2Ge_4O_{14}$, $Pb_3O(GeO_4)$, and Ge_2N_2O , are finally screened out from more than 100 germanates by two-step first-principles methods. Although the birefringence calculated by using the DFPT method of $Ba_2TiGe_2O_8$ is slightly smaller than the criteria, it exhibits a large band gap and giant SHG coefficients. Besides, the calculated Δn -SOS and Δn -DFTP are inconsistent. Therefore, it is worth to synthesize $Ba_2TiGe_2O_8$ for further measure and research. Finally, $Ba_2TiGe_2O_8$, $Pb_3Ga_2Ge_4O_{14}$, and $Pb_3O(GeO_4)$ were chosen to synthesize powder samples for further measurements. The phase purity was confirmed by powder XRD (Figure 9a-c). The TG and DSC curves for the three compounds are drawn in Figure S8.

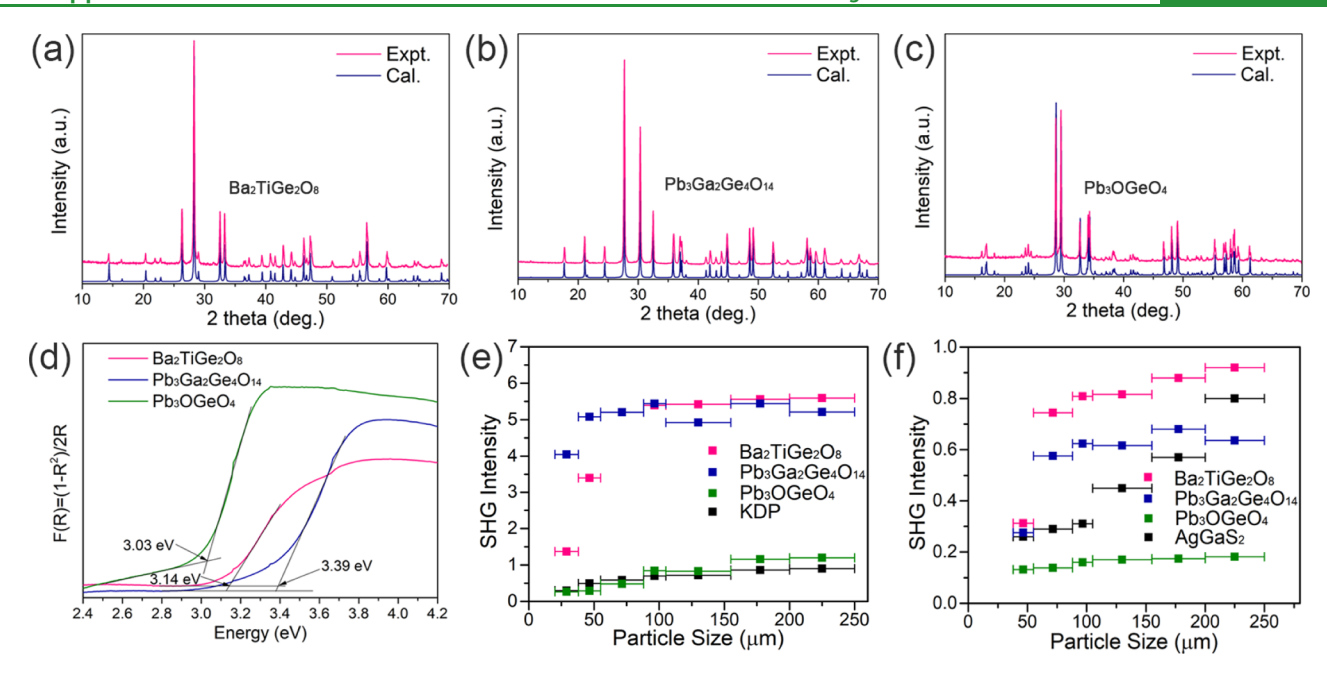


Figure 9. (a–c) Powder XRD patterns of the title compounds; (d) diffuse reflectance spectra for $Ba_2TiGe_2O_8$, $Pb_3Ga_2Ge_4O_{14}$, and $Pb_3O(GeO_4)$; (e–f) SHG intensities vs particle size of the title crystals compared with KDP at a 1064 nm incident laser and $AgGaS_2$ at a 2.09 μ m incident laser, respectively.

Ba₂TiGe₂O₈ exhibits a UV cutoff edge of 3.14 eV (Figure 9d). The PSHG measurement using the Kurtz-Perry method reveals that Ba₂TiGe₂O₈ has SHG intensities of 6.2 × KDP at 1064 nm fundamental wave laser radiation and 1.2 \times AgGaS₂ at 2.09 μ m fundamental wave laser radiation (particle size range: $200-250 \mu m$). To the best of our knowledge, it shows the largest SHG intensity among the reported germanates. It also suggests that Ba2TiGe2O8 is phase-matchable (Figure 9e,f). It is worth mentioning that PSHG intensity is a comprehensive reflection of all nonzero SHG tensors and related to point group and wavelength of incident laser.⁵¹ The experimental value of each tensor could be measured using a single crystal. Liu et al. reported the single crystal growth of $Ba_2TiGe_2O_8$ using the Czochraski method. The measurement of as-grown Ba₂TiGe₂O₈ shows a short UV cutoff edge around 300 nm and has a high transmittance in the wavelength range of 500-3000 nm. The PSHG test shows that it cannot achieve PM of 1064-532 nm because of small birefringence. The results are not consistent with the PSHG test in 1064-532 nm. Further measurements based on a single crystal are expected to settle the disagreement. Even the relative small birefringence still has chance to achieve PM in the mid-IR region as our experimental result in 2.09–1.045 μm because of small chromatic dispersion in the mid-IR region. Further precision measurement and more studies are expected to evaluate this crystal.

Langasite-type crystal $Pb_3Ga_2Ge_4O_{14}$ exhibits a UV cutoff edge of 3.39 eV (Figure 9d). PSHG intensities are 5.8 \times KDP and 0.8 \times AgGaS $_2$ at 1064 nm and 2.09 μm fundamental wavelength laser radiation (particle size range: 200–250 μm). The tendency of SHG intensities versus particle size reveals that $Pb_3Ga_2Ge_4O_{14}$ is phasematchable at two different incident lasers. Takahashi et al. synthesized the crystalline phase of $Pb_3Ga_2Ge_4O_{14}$ by crystallizing its glass. Their measurement indicates that $Pb_3Ga_2Ge_4O_{14}$ has the largest PSHG intensity among all the langasite-type crystals they studied. It is consistent with our prediction and measured results. Large-sized single crystals with high quality are required to measure refractive index and SHG tensors.

 $Pb_3O(GeO_4)$ shows a UV cutoff edge of 3.03 eV. It exhibits a relatively small PSHG intensity of 0.2 \times AgGaS $_2$ at 2.09 μm fundamental wavelength laser radiations. The predicted SHG coefficients do not match the experimental results. To find out the reasons, we first checked the crystal structure we used (ICSD coll. code 100275). The structure has an aberrant R-factor of 0.075 that

implies that the determined structure poorly represents the real structure. Coincidentally, another structure (ICSD coll. code 20197) with a lower R-factor of 0.053 described that the Pb₃O(GeO₄) crystal is disordered in which two-fifths oxygen atoms randomly occupy two different positions. This structure was excluded from our previous screening because of a disorder. As shown in Figure S9, the theoretical powder XRD patterns of the two structures are almost the same. However, the positions of the two strong peeks are exchanged for the two structures. It is interesting that the disordered structure matches the experimental XRD patterns well. Therefore, the structure is more likely to be disordered according to powder XRD results and our SHG intensity results. The poor-quality structure of Pb₃O(GeO₄) results in an inaccurate prediction of SHG coefficients. This case demonstrates that the experimental verification is indispensable to exclude the materials that give an inaccurate prediction of linear and nonlinear properties due to unreliable structures.

5. CONCLUSIONS

In summary, we developed a FHSP system to search for promising mid-IR NLO materials from germanates collected in ICSD. Four crystals including Ba₂TiGe₂O₈, Pb₃Ga₂Ge₄O₁₄, Pb₃O(GeO₄), and Ge₂N₂O are screened out from 128 structures. The powder samples of the three germanates are synthesized and tested. Ba₂TiGe₂O₈ exhibits a UV cutoff edge of 3.14 eV and strong phase-matchable SHG intensities of 1.2 \times AgGaS₂ at 2.09 μ m fundamental wave laser radiation. Pb₃Ga₂Ge₄O₁₄ exhibits a UV cutoff edge of 3.39 eV and PSHG intensities of $0.8 \times AgGaS_2$ at $2.09 \mu m$ fundamental wavelength laser radiations. The two crystals show the largest SHG intensity among the reported germanates to the best of our knowledge. The detailed study on the selected crystals with excellent NLO properties and statistical analysis for all structures show that the cations play an important role for SHG response and birefringence. The d⁰-TM and LP cations are significant sources for SHG and birefringence and are the preferred choice for exploring new NLO materials in germanates. The candidates screened out from ICSD would

give a guideline for the next step of crystal growth and exploring new mid-IR NLO materials.

ASSOCIATED CONTENT

Supporting Information

The Supporting Information is available free of charge at https://pubs.acs.org/doi/10.1021/acsami.0c15728.

Detailed information including chemical formula, ICSD number, SG, predicted band gap, birefringence, SHG tensors $\chi^{(2)}$ (pm/V), crystal structural representations and descriptions of all 128 structures, and TG and DSC of Ba₂TiGe₂O₈, Pb₃Ga₂Ge₄O₁₄, and Pb₃O(GeO₄) (PDF).

AUTHOR INFORMATION

Corresponding Authors

Bingbing Zhang — College of Chemistry and Environmental Science, Key Laboratory of Medicinal Chemistry and Molecular Diagnosis of the Ministry of Education, Chemical Biology Key Laboratory of Hebei Province, Hebei University, Baoding 071002, China; orcid.org/0000-0002-1334-5812; Email: zhangbb@hbu.edu.cn

Ying Wang — College of Chemistry and Environmental Science, Key Laboratory of Medicinal Chemistry and Molecular Diagnosis of the Ministry of Education, Chemical Biology Key Laboratory of Hebei Province, Hebei University, Baoding 071002, China; ⊙ orcid.org/0000-0001-6642-543X; Email: wangy@hbu.edu.cn

Authors

Jin Yu — College of Chemistry and Environmental Science, Key Laboratory of Medicinal Chemistry and Molecular Diagnosis of the Ministry of Education, Chemical Biology Key Laboratory of Hebei Province, Hebei University, Baoding 071002, China

Xiaodong Zhang — College of Chemistry and Environmental Science, Key Laboratory of Medicinal Chemistry and Molecular Diagnosis of the Ministry of Education, Chemical Biology Key Laboratory of Hebei Province, Hebei University, Baoding 071002, China

Kui Wu — College of Chemistry and Environmental Science, Key Laboratory of Medicinal Chemistry and Molecular Diagnosis of the Ministry of Education, Chemical Biology Key Laboratory of Hebei Province, Hebei University, Baoding 071002, China; orcid.org/0000-0001-8242-4613

Ming-Hsien Lee – Department of Physics, Tamkang University, New Taipei City 25137, Taiwan

Complete contact information is available at: https://pubs.acs.org/10.1021/acsami.0c15728

Funding

This work was supported by the National Natural Science Foundation of China (grant nos. 51702356, 52072109, 21975062, and 51872324), the Natural Science Foundation of Hebei Province (grant nos. B2019201433 and E2019201049), and the Advanced Talents Incubation Program of the Hebei University (grant no. 521000981279).

Notes

The authors declare the following competing financial interest(s): B.Z., J.Y., and X.Z. have filed a provisional patent application relating to this work.

The calculated results of all 128 germanates have been uploaded to our Nonlinear Optical Crystals First-Principles Database that is accessed by visiting http://nlo.hbu.cn.

ACKNOWLEDGMENTS

The authors thank Prof. Shilie Pan, Prof. Zhihua Yang, Dr. Qun Jing and Dr. Hao Li for helpful discussions and technical assistance.

REFERENCES

- (1) Liu, B.-W.; Zhang, M.-Y.; Jiang, X.-M.; Li, S.-F.; Zeng, H.-Y.; Wang, G.-Q.; Fan, Y.-H.; Su, Y.-F.; Li, C.; Guo, G.-C.; et al. Large Second-Harmonic Generation Responses Achieved by the Dimeric $\left[\text{Ge}_2\text{Se}_4(\mu\text{-Se}_2)\right]^4$ -Functional Motif in Polar Polyselenides $A_4\text{Ge}_4\text{Se}_{12}(A=\text{Rb},\text{Cs})$. Chem. Mater. 2017, 29, 9200–9207.
- (2) Bera, T. K.; Jang, J. I.; Song, J.-H.; Malliakas, C. D.; Freeman, A. J.; Ketterson, J. B.; Kanatzidis, M. G. Soluble Semiconductors AAsSe₂ (A = Li, Na) with a Direct-Band-Gap and Strong Second Harmonic Generation: A Combined Experimental and Theoretical Study. *J. Am. Chem. Soc.* **2010**, *132*, 3484–3495.
- (3) Lan, H.; Liang, F.; Jiang, X.; Zhang, C.; Yu, H.; Lin, Z.; Zhang, H.; Wang, J.; Wu, Y. Pushing Nonlinear Optical Oxides into the Mid-Infrared Spectral Region Beyond 10 μ m: Design, Synthesis, and Characterization of La₃SnGa₅O₁₄. *J. Am. Chem. Soc.* **2018**, *140*, 4684–4690.
- (4) Zhang, H.; Zhang, M.; Pan, S.; Dong, X.; Yang, Z.; Hou, X.; Wang, Z.; Chang, K. B.; Poeppelmeier, K. R. Pb₁₇O₈Cl₁₈: A Promising IR Nonlinear Optical Material with Large Laser Damage Threshold Synthesized in an Open System. *J. Am. Chem. Soc.* **2015**, *137*, 8360–8363.
- (5) Chen, J.; Hu, C.-L.; Mao, F.-F.; Feng, J.-H.; Mao, J.-G. A Facile Route for NLO Materials: Three-Site Alivolent Substitution Involving One Cation and Two Anions. *Angew. Chem., Int. Ed.* **2019**, *58*, 2098–2102.
- (6) Li, G.; Chu, Y.; Zhou, Z. From AgGaS₂ to Li₂ZnSiS₄: Realizing Impressive High Laser Damage Threshold Together with Large Second-Harmonic Generation Response. *Chem. Mater.* **2018**, *30*, 602–606.
- (7) Liang, F.; Kang, L.; Lin, Z.; Wu, Y.; Chen, C. Analysis and Prediction of Mid-IR Nonlinear Optical Metal Sulfides with Diamond-like Structures. *Coord. Chem. Rev.* **2017**, 333, 57–70.
- (8) Isaenko, L. I.; Yelisseyev, A. P. Recent Studies of Nonlinear Chalcogenide Crystals for the Mid-IR. *Semicond. Sci. Technol.* **2016**, 31, 123001.
- (9) Kang, L.; Ramo, D. M.; Lin, Z.; Bristowe, P. D.; Qin, J.; Chen, C. First Principles Selection and Design of Mid-IR Nonlinear Optical Halide Crystals. *J. Mater. Chem. C* **2013**, *1*, 7363–7370.
- (10) Lan, H.; Liang, F.; Lin, Z.; Yu, H.; Zhang, H.; Wang, J. Langasite Family Mid-Infrared Nonlinear Optical Oxide Materials: Structure, Property and Applications. *Int. J. Opt.* **2017**, 2017, 1–13.
- (11) Ohmer, M. C.; Pandey, R. Emergence of Chalcopyrites as Nonlinear Optical Materials. MRS Bull. 1998, 23, 16–22.
- (12) Chen, C.; Wu, Y.; Jiang, A.; Wu, B.; You, G.; Li, R.; Lin, S. New Nonlinear-Optical Crystal: LiB₃O₅. *J. Opt. Soc. Am. B* **1989**, *6*, 616.
- (13) Sasaki, T.; Mori, Y.; Yoshimura, M. Progress in the Growth of a CsLiB₆O₁₀ Crystal and Its Application to Ultraviolet Light Generation. *Opt. Mater.* **2003**, 23, 343–351.
- (14) Chen, C.; Wang, Y.; Xia, Y.; Wu, B.; Tang, D.; Wu, K.; Wenrong, Z.; Yu, L.; Mei, L. New Development of Nonlinear Optical Crystals for the Ultraviolet Region with Molecular Engineering Approach. *J. Appl. Phys.* **1995**, *77*, 2268–2272.
- (15) Chen, C.; Sasaki, T.; Li, R.; Wu, Y.; Lin, Z.; Mori, Y.; Hu, Z.; Wang, J.; Uda, S.; Yoshimura, M.; et al. *Nonlinear Optical Borate Crystals*; Wiley-VCH Verlag GmbH & Co. KGaA: Weinheim, Germany, 2012.
- (16) Boyd, G. D.; Miller, R. C.; Nassau, K.; Bond, W. L.; Savage, A. LiNbO₃: An Efficient Phase Matchable Nonlinear Optical Material. *Appl. Phys. Lett.* **1964**, *5*, 234–236.

- (17) Stolzenberger, R. A. Nonlinear Optical Properties of Flux Growth KTiOPO₄. Appl. Opt. 1988, 27, 3883–3886.
- (18) Bierlein, J. D.; Vanherzeele, H.; Ballman, A. A. Linear and Nonlinear Optical Properties of Flux-grown KTiOAsO4. *Appl. Phys. Lett.* **1989**, *54*, 783–785.
- (19) Xin, Y.; Lü, M.; Zhang, S.; Li, F. Nonlinear Optical Properties of Perfectly Polarized KIO₃ Single Crystal. *Chin. Phys. Lett.* **1992**, *9*, 77–78.
- (20) Weber, M. J. Handbook of Optical Materials; CRC Press: Boca Raton, 2002.
- (21) Xia, M.; Tang, C.; Li, R. Rb₄Li₂TiOGe₄O₁₂: A Titanyl Nonlinear Optical Material with the Widest Transparency Range. *Angew. Chem., Int. Ed.* **2019**, 58, 18257–18260.
- (22) Xu, J.; Wu, H.; Yu, H.; Zhang, W.; Hu, Z.; Wang, J.; Wu, Y.; Halasyamani, P. S. Li₂K₄TiOGe₄O₁₂: A Stable Mid-Infrared Nonlinear Optical Material. *Chem. Mater.* **2019**, *32*, 906–912.
- (23) Chen, C.; Ye, N.; Lin, J.; Jiang, J.; Zeng, W.; Wu, B. Computer-Assisted Design for Nonlinear Optical Crystals. *Adv. Mater.* **1999**, *11*, 1071.
- (24) Wu, Y.; Sasaki, T.; Nakai, S.; Yokotani, A.; Tang, H.; Chen, C. CsB₃O₅: A New Nonlinear Optical Crystal. *Appl. Phys. Lett.* **1993**, *62*, 2614–2615.
- (25) Xia, Y.; Chen, C.; Tang, D.; Wu, B. New Nonlinear Optical Crystals for UV and VUV Harmonic Generation. *Adv. Mater.* **1995**, *7*, 79–81
- (26) Chen, C.; Wang, Y.; Wu, B.; Wu, K.; Zeng, W.; Yu, L. Design and Synthesis of an Ultraviolet-Transparent Nonlinear Optical Crystal Sr,Be₂B₂O₇. *Nature* **1995**, 373, 322–324.
- (27) Yang, Z.; Lei, B.-H.; Zhang, W.; Pan, S. Module-Analysis-Assisted Design of Deep Ultraviolet Fluorooxoborates with Extremely Large Gap and High Structural Stability. *Chem. Mater.* **2019**, *31*, 2807–2813.
- (28) Lei, B.-H.; Yang, Z.; Yu, H.; Cao, C.; Li, Z.; Hu, C.; Poeppelmeier, K. R.; Pan, S. Module-Guided Design Scheme for Deep-Ultraviolet Nonlinear Optical Materials. *J. Am. Chem. Soc.* **2018**, 140, 10726–10733.
- (29) Zhang, B.; Zhang, X.; Yu, J.; Wang, Y.; Wu, K.; Lee, M.-H. First-Principles High-Throughput Screening Pipeline for Nonlinear Optical Materials: Application to Borates. *Chem. Mater.* **2020**, *32*, 6772–6779
- (30) Perdew, J. P.; Burke, K.; Ernzerhof, M. Generalized Gradient Approximation Made Simple. *Phys. Rev. Lett.* **1996**, *77*, 3865–3868.
- (31) Clark, S. J.; Segall, M. D.; Pickard, C. J.; Hasnip, P. J.; Probert, M. I. J.; Refson, K.; Payne, M. C. First Principles Methods Using CASTEP. Z. Kristallogr.-Cryst. Mater. 2005, 220, 567–570.
- (32) Zhang, Z.; Wang, Y.; Zhang, B.; Yang, Z.; Pan, S. Polar Fluorooxoborate, NaB₄O₆F: A Promising Material for Ionic Conduction and Nonlinear Optics. *Angew. Chem., Int. Ed.* **2018**, *57*, 6577–6581.
- (33) Yang, Z.; Huang, X.; Liu, Q.; Hou, D.; Zhang, B.; Huang, S.; Pan, S.; Yang, Y.; Zhang, M. Cation Effect Investigation on Electronic Structure, Magnetic and Optical Properties of Li₂Pb₂CuB₄O₁₀. *Chem. Phys.* **2015**, *447*, 60–63.
- (34) Zhang, B.; Shi, G.; Yang, Z.; Zhang, F.; Pan, S. Fluorooxoborates: Beryllium-Free Deep-Ultraviolet Nonlinear Optical Materials without Layered Growth. *Angew. Chem., Int. Ed.* **2017**, *56*, 3916–3919.
- (35) Zhang, B.; Han, G.; Wang, Y.; Chen, X.; Yang, Z.; Pan, S. Expanding Frontiers of Ultraviolet Nonlinear Optical Materials with Fluorophosphates. *Chem. Mater.* **2018**, *30*, 5397–5403.
- (36) Wu, K.; Zhang, B.; Yang, Z.; Pan, S. New Compressed Chalcopyrite-like Li₂BaMIVQ₄(MIV= Ge, Sn; Q = S, Se): Promising Infrared Nonlinear Optical Materials. *J. Am. Chem. Soc.* **2017**, 139, 14885−14888.
- (37) Wang, X.; Wang, Y.; Zhang, B.; Zhang, F.; Yang, Z.; Pan, S. CsB₄O₆F: A Congruent-Melting Deep-Ultraviolet Nonlinear Optical Material by Combining Superior Functional Units. *Angew. Chem., Int. Ed.* **2017**, *56*, 14119–14123.

- (38) Shi, G.; Wang, Y.; Zhang, F.; Zhang, B.; Yang, Z.; Hou, X.; Pan, S.; Poeppelmeier, K. R. Finding the Next Deep-Ultraviolet Nonlinear Optical Material: NH₄B₄O₆F. *J. Am. Chem. Soc.* **2017**, *139*, 10645–10648
- (39) Mutailipu, M.; Zhang, M.; Zhang, B.; Wang, L.; Yang, Z.; Zhou, X.; Pan, S. $SrB_5O_7F_3$ Functionalized with $[B_5O_9F_3]^{6-}$ Chromophores: Accelerating the Rational Design of Deep-Ultraviolet Nonlinear Optical Materials. *Angew. Chem., Int. Ed.* **2018**, *57*, 6095–6099.
- (40) Chen, X.; Zhang, B.; Zhang, F.; Wang, Y.; Zhang, M.; Yang, Z.; Poeppelmeier, K. R.; Pan, S. Designing an Excellent Deep-Ultraviolet Birefringent Material for Light Polarization. *J. Am. Chem. Soc.* **2018**, 140, 16311–16319.
- (41) Nicholls, R. J.; Morris, A. J.; Pickard, C. J.; Yates, J. R. OptaDOS A New Tool for EELS Calculations. *J. Phys.: Conf. Ser.* **2012**, *371*, 012062.
- (42) Morris, A. J.; Nicholls, R. J.; Pickard, C. J.; Yates, J. R. OptaDOS: A Tool for Obtaining Density of States, Core-Level and Optical Spectra from Electronic Structure Codes. *Comput. Phys. Commun.* **2014**, *185*, 1477–1485.
- (43) Read, A. J.; Needs, R. J. Calculation of Optical Matrix Elements with Nonlocal Pseudopotentials. *Phys. Rev. B: Condens. Matter Mater. Phys.* **1991**, *44*, 13071.
- (44) Aversa, C.; Sipe, J. E. Nonlinear Optical Susceptibilities of Semiconductors: Results with a Length-Gauge Analysis. *Phys. Rev. B: Condens. Matter Mater. Phys.* **1995**, *52*, 14636.
- (45) Zhang, B.; Lee, M.-H.; Yang, Z.; Jing, Q.; Pan, S.; Zhang, M.; Wu, H.; Su, X.; Li, C.-S. Simulated Pressure-Induced Blue-Shift of Phase-Matching Region and Nonlinear Optical Mechanism for $K_3B_6O_{10}X$ (X = Cl, Br). *Appl. Phys. Lett.* **2015**, *106*, 031906.
- (46) Lin, J.; Lee, M.-H.; Liu, Z.-P.; Chen, C.; Pickard, C. J. Mechanism for Linear and Nonlinear Optical Effects in β BaB₂O₄ Crystals. *Phys. Rev. B: Condens. Matter Mater. Phys.* **1999**, *60*, 13380.
- (47) Krukau, A. V.; Vydrov, O. A.; Izmaylov, A. F.; Scuseria, G. E. Influence of the Exchange Screening Parameter on the Performance of Screened Hybrid Functionals. *J. Chem. Phys.* **2006**, *125*, 224106.
- (48) Heyd, J.; Scuseria, G. E.; Ernzerhof, M. Hybrid Functionals Based on a Screened Coulomb Potential. *J. Chem. Phys.* **2003**, *118*, 8207–8215.
- (49) Jia, W.; Fu, J.; Cao, Z.; Wang, L.; Chi, X.; Gao, W.; Wang, L.-W. Fast Plane Wave Density Functional Theory Molecular Dynamics Calculations on Multi-GPU Machines. *J. Comput. Phys.* **2013**, 251, 102–115.
- (50) Jia, W.; Cao, Z.; Wang, L.; Fu, J.; Chi, X.; Gao, W.; Wang, L.-W. The Analysis of a Plane Wave Pseudopotential Density Functional Theory Code on a GPU Machine. *Comput. Phys. Commun.* **2013**, *184*, 9–18.
- (51) Kurtz, S. K.; Perry, T. T. A Powder Technique for the Evaluation of Nonlinear Optical Materials. *J. Appl. Phys.* **1968**, *39*, 3798–3813.
- (52) Payne, D. J.; Egdell, R. G.; Walsh, A.; Watson, G. W.; Guo, J.; Glans, P.-A.; Learmonth, T.; Smith, K. E. Electronic Origins of Structural Distortions in Post-Transition Metal Oxides: Experimental and Theoretical Evidence for a Revision of the Lone Pair Model. *Phys. Rev. Lett.* **2006**, *96*, 157403.
- (53) Walsh, A.; Payne, D. J.; Egdell, R. G.; Watson, G. W. Stereochemistry of Post-Transition Metal Oxides: Revision of the Classical Lone Pair Model. *Chem. Soc. Rev.* **2011**, *40*, 4455–4463.
- (54) Grins, J.; Werner, P.-E.; Hellberg, S.; Sjöström, M.; Wold, S.; Colacio, E.; Mulichak, A. M.; Alminger, T.; Erickson, M.; Grundevik, I.; Hagin, I.; Hoffman, K.-J.; Johansson, S.; Larsson, S.; Löfberg, I.; Ohlson, K.; Persson, B.; Skånberg, I.; Tekenbergs-Hjelte, L. The Crystal Structure and Ionic Conductivity Properties of K₂ZnGe₂O₆. *Acta Chem. Scand.* **1989**, *43*, 11–14.
- (55) Rulmont, A.; Tarte, P.; Winand, J. M. Vibrational Spectrum of Crystalline and Glassy LiBGeO₄: Structural Analogies with BAsO₄. *J. Mater. Sci. Lett.* **1987**, *6*, 659–662.
- (56) Liebertz, J.; Stähr, S. Züchtung Und Untersuchung von LiBGeO₄-Einkristallen. Z. Kristallogr.-Cryst. Mater. **1981**, 155, 115–120.

- (57) Parise, J. B.; Gier, T. E. Hydrothermal Syntheses and Structural Refinements of Single Crystal LiBGeO4 and LiBSiO4. *Chem. Mater.* **1992**, *4*, 1065–1067.
- (58) Liu, Q.; Hu, C.; Su, X.; Abudoureheman, M.; Pan, S.; Yang, Z. LiGeBO₄: A Nonlinear Optical Material with a Balance between Deep-Ultraviolet Cut-off Edge and Large SHG Response Induced by Hand-in-Hand Tetrahedra. *Inorg. Chem. Front.* **2019**, *6*, 914–919.
- (59) Becker, P. Crystal Growth, Thermal and Linear Optical Properties of LiGeBO₄. Cryst. Res. Technol. **2001**, 36, 119–126.
- (60) Liu, X.; Huo, L.; Liao, B.; Wei, Q.; Hu, X.; Zhuang, N.; Chen, J.; Huang, L.; Zhang, G. Czochraski Growth, Defect Analysis and Refractive Index of Ba₂TiGe₂O₈ Crystal with Excellent Optical Nonlinearities. *Opt. Mater.* **2015**, 42, 361–365.
- (61) Takahashi, Y.; Saitoh, K.; Benino, Y.; Fujiwara, T.; Komatsu, T. Formation of Langasite-Type Crystals in Corresponding Glasses and Their Second-Order Optical Nonlinearities. *J. Ceram. Soc. Jpn.* **2004**, *112*, 61–64.